Endometriosis-Associated Mesenchymal Stem Cells Support Ovarian Clear Cell Carcinoma through Iron Regulation

Huda I. Atiya[1], Leonard Frisbie[2], Ester Goldfeld[3], Taylor Orellana[4], Nicole Donnellan[5], Francesmary Modugno[5], Michael Calderon[6], Simon Watkins[6], Rugang Zhang[7], Esther Elishaev[8], Thing Rinda Soong[8], Anda Vlad[4], and Lan Coffman[1,4]

ABSTRACT

Ovarian clear cell carcinoma (OCCC) is a deadly and treatment-resistant cancer, which arises within the unique microenvironment of endometriosis. In this study, we identified a subset of endometriosis-derived mesenchymal stem cells (enMSC) characterized by loss of CD10 expression that specifically support OCCC growth. RNA sequencing identified alterations in iron export in CD10-negative enMSCs and reciprocal changes in metal transport in cocultured OCCC cells. CD10-negative enMSCs exhibited elevated expression of iron export proteins hephaestin and ferroportin and donate iron to associated OCCCs, functionally increasing the levels of labile intracellular iron. Iron is necessary for OCCC growth, and CD10-negative enMSCs prevented the growth inhibitory effects of iron chelation. In addition, enMSC-mediated increases in OCCC iron resulted in a unique sensitivity to ferroptosis. *In vitro* and *in vivo*, treatment with the ferroptosis inducer erastin resulted in significant death of cancer cells grown with CD10-negative enMSCs. Collectively, this work describes a novel mechanism of stromal-mediated tumor support via iron donation. This work also defines an important role of endometriosis-associated MSCs in supporting OCCC growth and identifies a critical therapeutic vulnerability of OCCC to ferroptosis based on stromal phenotype.

Significance: Endometriosis-derived mesenchymal stem cells support ovarian clear cell carcinoma via iron donation necessary for cancer growth, which also confers sensitivity to ferroptosis-inducing therapy.

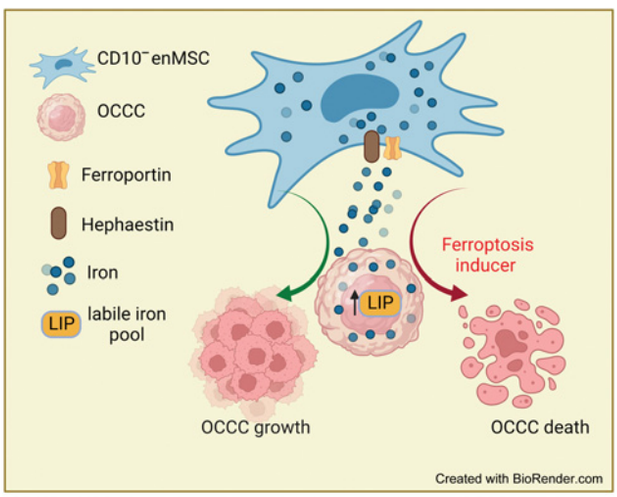

CD10⁻ enMSCs donate iron to support ovarian clear cell cancer (OCCC) growth while creating a unique susceptibility to ferroptosis

Introduction

Ovarian cancer is collectively the most deadly gynecologic malignancy in the United States (1). However, ovarian cancer encompasses a diverse set of histologic subtypes, which demonstrate dramatic differences in molecular profile, proposed site of origin, and clinical outcome. Ovarian clear cell carcinoma (OCCC) is one of the most aggressive and understudied subtypes of ovarian cancer. When diagnosed in advanced stages (stage III or IV), OCCC has an almost 2-fold increased mortality compared with the most common subtype, high-grade serous ovarian cancer (HGSC; ref. 2). OCCC has a distinct molecular profile characterized by *ARID1A* mutations and commonly co-occurring *PI3K* and *PTEN* mutations (3). Although the preponderance of evidence points to a fallopian tube origin of HGSC, OCCC is thought to arise within sites of endometriosis (4). Endometriosis, an inflammatory disease marked by ectopic growth of uterine tissue containing both epithelial and stromal components, is a known risk factor for OCCC. Indeed, women with histologically proven endometriosis involving the ovary have a 2.3-fold increased risk of OCCC (5). The

[1]Division of Hematology/Oncology, Department of Medicine, Hillman Cancer Center, University of Pittsburgh, Pittsburgh, Pennsylvania. [2]Department of Integrative Systems Biology, University of Pittsburgh, Pittsburgh, Pennsylvania. [3]University of Pittsburgh School of Medicine, University of Pittsburgh, Pittsburgh, Pennsylvania. [4]Division of Gynecologic Oncology, University of Pittsburgh, Pittsburgh, Pennsylvania. [5]Department of Obstetrics, Gynecology, and Reproductive Sciences, Magee Women's Research Institute, University of Pittsburgh, Pittsburgh, Pennsylvania. [6]Center for Biologic Imaging, University of Pittsburgh, Pittsburgh, Pennsylvania. [7]Immunology, Microenvironment and Metastasis Program, The Wistar Institute, Philadelphia, Pennsylvania. [8]Department of Pathology, University of Pittsburgh, Pittsburgh, Pennsylvania.

Corresponding Author: Lan Coffman, Department of Medicine, University of Pittsburgh Medical Center, 204 Craft Avenue, Pittsburgh, PA, 15213. E-mail: coffmanl@upmc.edu

Cancer Res 2022;82:4680–93

doi: 10.1158/0008-5472.CAN-22-1294

This open access article is distributed under the Creative Commons Attribution-NonCommercial-NoDerivatives 4.0 International (CC BY-NC-ND 4.0) license.

©2022 The Authors; Published by the American Association for Cancer Research

endometriosis microenvironment is marked by inflammatory changes and high levels of iron due to continued menstrual cycling of the epithelial lining (6). Both chronic inflammation and high levels of iron are risk factors for cancer development; however, the mechanisms by which the endometriotic microenvironment supports OCCC formation and growth are largely unknown (7, 8).

Previous work focused on HGSC demonstrated that a key stromal component in the tumor microenvironment (TME), the carcinoma-associated mesenchymal stem cell (CA-MSC), strongly supports ovarian cancer growth (9). These CA-MSCs arise from normal tissue MSCs, which become cancer-educated to support ovarian cancer survival, growth, and spread (10). MSCs are also readily present within both endometrial and endometriosis tissue and may be critical to the formation of endometriosis (11). Here we report the discovery of a subset of endometriosis-derived MSCs (enMSC), which specifically support OCCC growth and metastasis. OCCC-supportive enMSCs are marked by loss of CD10 expression. CD10 negative ($CD10^-$) enMSCs increase OCCC proliferation, chemotherapy resistance, sphere formation, and *in vivo* tumor growth. Mechanistically, $CD10^-$ enMSCs increase labile iron within tumor cells (TC) necessary for OCCC growth. However, this creates a unique susceptibility to ferroptosis. Treatment with a ferroptosis inducer, erastin, specifically kills OCCC grown with $CD10^-$ enMSCs, thus presenting a potentially powerful therapeutic target.

Materials and Methods

enMSCs

enMSCs were isolated from primary human benign endometriosis deposits involving the ovary or fallopian tubes obtained from the surgical resection specimens of females (including cisgender, transgender, and nonbinary individuals) undergoing surgery for benign indications in accordance with protocols approved by the University of Pittsburgh's Institutional Review Board (PRO17080326). Written informed consent was obtained from all patients. MSCs were isolated following previously described protocols (9,12). Clinical characteristics provided in Supplementary Table S1. Briefly, dissociated cells were plated in mammary epithelial cell basal medium (MEBM) supplemented with 10% heat-inactivated FBS, 1× B27, 20 ng/mL EGF, 1 ng/mL hydrocortisone, 5 μg/mL insulin, 100 μmol/L β-mercaptoethanol, 10 ng/mL β-fibroblast growth factor (FGF), 1% penicillin/streptomycin, and 20 μg/mL gentamicin. MSCs were selected for plastic adherence and cell surface marker expression CD105 (BD Biosciences, Catalog No. 561443, RRID:AB_10714629) CD90 (BD Biosciences, Catalog No. 555596, RRID:AB_395970), CD73 (BD Biosciences, Catalog No. 560847, RRID:AB_10612019) positive; CD45 (BD Biosciences, Catalog No. 340664, RRID:AB_400074), CD34 (BD Biosciences, Catalog No. 555824, RRID:AB_398614), CD14 (BD Biosciences, Catalog No. 340436, RRID:AB_400509), and CD19 (BD Biosciences, Catalog No. 340364, RRID:AB_400018) negative. Adipocyte, osteocyte, and chondrocyte differentiation capacity was verified (following guidelines presented by the ISCT on the minimal criteria for defining multipotent mesenchymal stem cells; ref. 13) and as described previously (9,12,14). MSCs ($CD10_{high}$ or $CD10_{low}$) were propagated for <8–10 passages and used for functional experiments at passage 5 or below. Each MSC sample was derived from an individual patient and the individual patient MSC samples were maintained separately. All experiments were performed with at least three MSC samples from independent patients to account for intrapatient heterogeneity.

Ovarian clear cell carcinoma cell lines

The TOV-21G cell line was purchased from ATCC (RRID: CVCL_3613) and maintained in a 1:1 mixture of MCDB 105 medium and Medium 199 supplemented with 15% FBS. The OVISE cell line was a kind gift of Dr. R Zhang and was maintained in RPMI1640 medium supplemented with 10% FBS and penicillin/streptomycin (penicillin: 100 units/mL, streptomycin: 0.1 mg/mL). The RMG1 cell line was a kind gift of Dr. R. Zhang and maintained in DMEM/F12 medium supplemented with 10% FBS and penicillin/streptomycin (penicillin: 100 units/mL, streptomycin: 0.1 mg/mL). All three OCCC lines were cultured at 37°C in a 5% CO2 humidified incubator.

High-grade serous carcinoma cell lines

Human ovarian HGSC cell line OVCAR3 (RRID: CVCL_0465) were purchased through ATCC. The primary patient derived HGSC cell line, PT412, and OVSAHO cell line was a kind gift from Dr. R. Buckanovich. All cells were maintained in DMEM medium supplemented with 10% FBS and penicillin/streptomycin (penicillin: 100 units/mL, streptomycin: 0.1 mg/mL). Cells were cultured at 37°C in a 5% CO_2 humidified incubator.

All cancer cell lines have been validated using STR testing though ATCC and all cells are tested on a bimonthly basis to verify *Mycoplasma* negativity (last test 8/2022). Cells were used at passage 10 or less from thawing.

Flow cytometry–based cell sorting

enMSCs were stained with APC conjugated anti-CD10 antibody (Thermo Fisher Scientific, Catalog No. 17–0106–42, RRID: AB_11043552) for 20 minutes, followed by washing with PBS. Cells were then resuspended in PBS with 2% FBS and sorted into $CD10^+$ and $CD10^-$ populations with gating based on APC-IgG control using The BD FACSAria Fusion system. Sorted cells were collected directly into supplemented MEBM.

Proliferation, chemoresistance, and ferroptosis induction assays

OCCC lines were stained with CellTrace Violet (CTV - Invitrogen C34571) following the manufacturer's protocol. Briefly, cells were washed once with PBS and resuspended in PBS at 1×10^6 cells/mL, followed by staining with 1 μL (5 mmol/L) of CTV per 1×10^6 cells for 25 minutes. Cells were then centrifuged and resuspended in fresh complete culture medium.

1×10^4 CTV-labeled OCCC cells were cultured alone, with 1×10^4 $CD10_{low}$ enMSCs, or with 1×10^4 $CD10_{high}$ enMSCs in a 12-well plate. For the chemoresistance assay, Cisplatin was added to the culture medium at 0.5, 1, and 2 μg/mL concentrations. For ferroptosis induction assay, erastin (MedChemExpress- HY-15763/CS-1675) or dihydroartemisinin (DHA; Sigma-Aldrich D7439) was added to the culture medium at 0.5, 1, 2, 5, and 10 μmol/L. The OCCC cell numbers were followed for 4 days. Cells were collected from 2 wells per condition per day and counted using a hemocytometer. Flow cytometric analysis was used to determine the percentage of the CTV-labeled TC to quantify viable TCs per condition. Total OCCC cells (CTV-labeled) = total cell number × CTV positive cell %.

Sphere formation assay

OCCC lines were stained with CellTrace Yellow (CTY - Invitrogen C34573), following the manufacturer's protocol (CTY falls in the "orange/red" spectrum for microscopy). Briefly, cells were washed once with PBS and resuspended in PBS at 1×10^6 cells/mL, followed by staining with 5 mmol/L of CTY per 1×10^6 cells

for 25 minutes. Cells were then centrifuged and resuspended in fresh complete culture medium. Using ultra-low-adherent 96-well plates, labeled OCCC cells were plated alone (1×10^3 cells/well), with $CD10_{low}$ enMSCs (0.5×10^3 OCCC cells + 0.5×10^3 enMSCs/well), or with $CD10_{high}$ enMSCs (0.5×10^3 OCCC cells + 0.5×10^3 enMSCs/well) in 300 μL MSC media (described above). After 7 days, total spheres (defined as >4 cells spheroid, at least 1 TC per sphere) in the entire well were counted.

Quantitative real-time PCR

RNA was isolated using RNeasy Mini Kit and on-column DNase treatment (Qiagen, 28106). After determining the RNA concentration using the Nano-Drop ND-1000 Spectrophotometer, cDNA was synthesized using SuperScript III First Strand Synthesis System (random hexamer; Invitrogen, 18080–051). SYBR-green based RT-qPCR (Applied Biosystem, 4472908) was performed using CFX96 Real-Time System, samples were run for 40 cycles with GAPDH as the reference gene. Primer sequences are listed in Supplementary Table S2.

RNA sequencing

RNA extraction and sample quality control

Total RNA was extracted using a NucleoSpin RNA Kit (Machery-Nagel) and eluted in nuclease-free water. RNA concentration and quality was assessed via a NanoDrop spectrophotometer (Thermo Fisher Scientific). Samples were then packaged and shipped to Novogene (Novogene Corporation) for further processing and sequencing.

Library construction and sequencing

mRNA was purified from total RNA using poly-T oligo-attached magnetic beads. After fragmentation, first-strand cDNA synthesis was carried out using random hexamer primers followed by second strand synthesis using dUTP. Qubit (Thermo Fisher Scientific) and real-time PCR was used for quantification and bioanalyzer for size distribution detection. Quantified libraries were pooled and sequenced on an Illumina platform (Illumina Inc.) and paired-end reads were generated.

QC, read mapping, and differential expression analysis

Raw reads in fastq format were processed through a Novogene in-house perl script for QC. Briefly, reads containing adapters, ploy-N, and low-quality reads were removed and Q20, Q30, and GC content was calculated. The index of the reference genome hg38 was built and paired-end clean reads were aligned to the reference genome using hisat2 (v2.0.5; ref. 15). Quantification of the gene expression level was done via featureCounts (v1.5.0-p3; ref. 16). The FPKM of each gene was calculated based on the length of the gene and read counts mapped to the gene. Differential gene expression analysis was performed using the DESeq2 R package (v1.20.0; ref. 17). Resulting *P* values were adjusted using the Benjamini–Hochberg method to control for FDR. Genes with a $P_{adj} \Leftarrow 0.05$ and $|\log2(\text{FoldChange})| \geq 1$ were assigned as differentially expressed.

Functional analysis

Over-representation analysis (ORA) using gene ontology (GO) terms was done on the differentially expressed gene (DEG) lists obtained from DESeq2 using the clusterProfiler package in R version 4.1.2 (18). Briefly, genes with a log2 fold change greater or lesser than 1 were matched to GO terms and tested for over-representation against the "org.Hs.eg.db" gene universe using the *enrichGO* function. GO terms with a Benjamini–Hochberg corrected *P* values with a cutoff of 0.1 were obtained. Redundant GO terms were removed from the ORA result using Revigo, which finds a representative subset of GO terms using a clustering algorithm based on semantic similarity measures (19). Results were visualized via the *dotplot* function in clusterProfiler (18).

Mouse models

All experimental procedures were performed in accordance with the approved protocol by the Institutional Animal Care and Use Committee (IACUC) at the University of Pittsburgh (PRO21018732). 6- to 8-week-old female NSG (NOD SCID gamma; The Jackson Laboratory, Catalog No. 005557; RRID:IMSR_JAX:005557) mice were used for mouse models.

Subcutaneous mouse model

A total of 2×10^5 TOV-21G cells were injected alone, with $CD10_{low}$ enMSCs (2×10^5), or with $CD10_{high}$ enMSCs (2×10^5) subcutaneously into the mammary fat pad of NSG mice (total injection volume was 100 μL), with 5 mice used for each of the three conditions. Initial engraftment was assessed at 2 weeks post-injection and only mice with established tumors at this time point were followed for tumor volume/growth assessment. Mouse weight and health were monitored throughout the experiment, and the end point was determined when the first group of mice met the endpoint criteria (>10% weight loss, >20% weight gain, tumor size >1,000 mm^3, ulceration or distress). Mice were then sacrificed, and a necropsy was performed on each mouse to assess for metastasis.

Orthotopic mouse model

2×10^5 TOV-21G luciferase labeled cells were injected alone, with $CD10_{low}$ enMSCs (2×10^5), or with $CD10_{high}$ enMSCs (2×10^5; total injection volume was in <15 μL) into the ovarian bursa of NSG mice, with 10 mice used for each of the three conditions. Tumor growth and metastatic progression were monitored bi-weekly using In Vivo Imaging System (IVIS) as described previously [9,12]. Mouse weight and health were monitored over time. Mice were followed for survival and individual mice were sacrificed as they met the end-point criteria as above. A necropsy was performed on each mouse to assess the metastatic burden.

Immunoblotting

Using RIPA buffer (Pierce, 89900), cell pellets were homogenized with a complete protease inhibitor cocktail. Samples were then centrifuged at 16,000 × *g* at 4°C for 15 minutes to remove insoluble material. Protein concentrations were determined using the Pierce BCA Protein Assay Kit (Thermo Fisher Scientific, 23227). Using 4% to 12% NuPAGE SDS gel (Invitrogen), equal amounts of protein were separated and transferred onto a PVDF membrane. Anti-ferritin L (Abcam, Catalog No. ab69090, RRID: AB_1523609), anti-ferritin H (Abcam, Catalog No. ab65080, RRID: AB_10564857), anti-Ferroportin (Abcam, Catalog No. ab58695, RRID:AB_2302072), and anti-transferrin receptor (Abcam, Catalog No. ab84036, RRID:AB_10673794) at 1:1,000 dilution, and anti-HEPH at 1:500 dilution (Abcam, Catalog No. ab108003, RRID: AB_10863278) were used. Bands were visualized using the Super-Signal West Pico PLUS Chemiluminescent Substrate (Pierce, 34577).

Labile iron pool assay

Intracellular (labile) iron pool was quantified as described previously (20). Briefly, 1×10^5 CTV-labeled OCCC cells were cultured

alone, with 2×10^5 $CD10_{low}$ enMSCs, or with 2×10^5 $CD10_{high}$ enMSCs. At day 3, cells were collected and washed twice with PBS. Cells were then incubated with 0.125 μmol/L calcein AM (CA-AM; Invitrogen-C1430) for 15 minutes at 37ºC. After washing with PBS, cells were incubated for 15 minutes with DFO at 100 mmol/L. Cells were then washed with PBS and analyzed by flow cytometry at a rate of 1,000 events/second at 448 nm excitation. Mean fluorescence intensity (MFI) was calculated using FlowJo. Given that CA-AM fluorescence intensity increases as free iron content decreases, the change of MFI represents the free iron pool (labile iron pool, LIP).

ΔMFI = MFICA - AM/DFO - MFICA - AM alone

4-Hydroxynonenal staining

A total of 2×10^4 CTV-labeled OCCC cells were cultured alone, with 2×10^4 $CD10^-$ enMSCs, or with 2×10^4 $CD10^+$ enMSCs on a coverslip in a 6-well plate. Erastin was added to the culture medium at 1 μmol/L. Day 3 after the coculture, cells were fixed and incubated with anti-4-hydroxynonenal (4-HNE; Millipore, Catalog No. AB5605, RRID: AB_569332) overnight at 4°C. After washing with PBB (0.5% BSA in PBS), cells were incubated with Alexa Fluor 546 conjugated secondary antibody (Thermo Fisher Scientific, Catalog No. A-11056, RRID: AB_2534103) for 1 hour at room temperature.

BODIPY assay

BODIPY 581/591 C11 was used to detect ferroptosis as described previously (21). Briefly, 4×10^4 CTV-labeled OCCC cells were cultured alone, with 4×10^4 $CD10^-$ enMSCs, or with 4×10^4 $CD10^+$ enMSCs in a 6-well plate. Erastin was added to the culture medium at 1 μmol/L. After 24 hours of erastin treatment, 2 μL of 1.5 mmol/L BODIPY-C11 stock solution was added to erastin-treated cells (no erastin treatment cells were used as a control). Cells were then returned to the tissue culture incubator and allowed to stain with BODIPY for 20 minutes. After washing with HBSS buffer, cells were then harvested for flow analysis using The BD FACSAriaTM Fusion system.

Ferric ammonium citrate treatment

A total of 1×10^4 TOV-21G cells were cultured per well in 12-well plates. Ferric ammonium citrate (FAC; MP Biomedicals, 158040) was added to the culture media at 0, 0.05, 0.1, and 0.2 μmol/L. Cells were collected from 2 wells per condition per day and counted using a hemocytometer with trypan blue exclusion.

Statistical analysis

Data are presented as mean ± SEM. All experiments were performed on three ovarian clear cell cancer lines and on at least three patient-derived enMSCs. To determine the statistical significance, Student unpaired *t* test, ANOVA or log-rank (Mantel–Cox) test were used.

Data availability

The data generated in this study are available upon request from the corresponding author.

Results

MSCs are present within endometriosis tissue and within the OCCC TME

As OCCC is thought to arise within endometriosis and MSCs within the TME support other ovarian cancer histologic subtypes, we first assessed the prevalence of MSCs within endometriosis derived from fresh benign endometriosis samples from women undergoing surgery for noncancer-related indications (Supplementary Table S1; refs. 9, 10, 14). We found that endometriosis contains a clearly discernible population of MSCs (as defined by the international society of cellular therapy; ref. 13). We quantified the prevalence of MSCs as a percentage of total viable cells by dissociating the tissue into single cell suspension and analyzing cells using flow cytometry to define the MSCs as CD73/CD90/CD105 positive and CD45/CD34/CD14/CD11b/CD19 negative. MSCs were isolated in parallel as described previously, verifying plastic adherence and trilineage differentiation into adipocytes, osteocytes, and chondrocytes (Supplementary Fig. S1; refs. 9, 12). Given the variability in MSC prevalence within specific organs, we specifically analyzed endometriosis involving the ovary or fallopian tube. We identified MSCs present within all 15 patient samples of endometriosis. We compared the prevalence of MSCs in endometriosis deposits within ovary or fallopian tube tissue to normal ovary or fallopian tubes without endometriosis (or other pathology). At both organ sites, tissues with endometriosis had a significantly higher number of MSCs (**Fig. 1A**). We also assessed OCCC involving the ovary or fallopian tube and demonstrated that OCCC contained high levels of MSCs consistent with our previous work describing the increased prevalence of MSCs in cancer versus normal tissue (10). Interestingly, the proportion of MSCs within endometriosis tissue was equivalent to the proportion of MSCs within OCCC at both organ sites (**Fig. 1A**).

A subset of MSCs support OCCC growth

We next tested the functional impact of enMSCs on OCCC growth. After isolating and verifying MSCs from 15 endometriosis samples, we cocultured these MSCs with TOV-21G OCCC cells. Interestingly, the impact on growth rate was mixed with a subset of MSCs supporting OCCC growth and a subset of MSCs with no effect or even slight suppression of OCCC growth (**Fig. 1B**). Intrigued by this result, we assessed known MSC and endometrial stromal surface markers to determine if there was heterogeneity among the populations. MSC markers were identical across the cell lines consistent with all cells meeting the identity of a MSC (Supplementary Fig. S1B). However, we found significant alterations in the endometrial stromal marker, CD10 (**Fig. 1C**). CD10 is generally ubiquitously expressed on endometrial stromal cells (22). However, MSCs that promoted OCCC growth demonstrated a significantly lower proportion of cells with CD10 surface expression. This was further confirmed at the transcript level as MSCs with low surface CD10 expression similarly demonstrated decreased levels of CD10 mRNA (**Fig. 1D** and **E**). We also directly evaluated the proportion of enMSCs with and without CD10 surface expression from five additional endometriosis tissues (involving the ovary) demonstrating $CD10^-$ enMSCs made up 1% to 5% of the total viable cells isolated from the patient samples (Supplementary Fig. S1C). We next assessed the CD10 surface expression of MSCs derived from ovarian clear cell cancer samples. The majority of MSCs derived from primary OCCC were negative for CD10 surface expression (**Fig. 1D**).

On the basis of the above findings, we grouped the enMSCs into $CD10_{high}$ versus $CD10_{low}$ populations (using a threshold of <40% of the enMSC population expressing CD10 for the "low" population and >60% for the "high" population). We confirmed the dichotomous impact of enMSCs on OCCC growth with $CD10_{low}$ populations, supporting OCCC growth in all three lines tested and $CD10_{high}$ populations restricting OCCC growth in TOV-21G and OVISE and having no impact on RMG1 growth. This was confirmed with eight independent patient-derived enMSCs with three independent OCCC

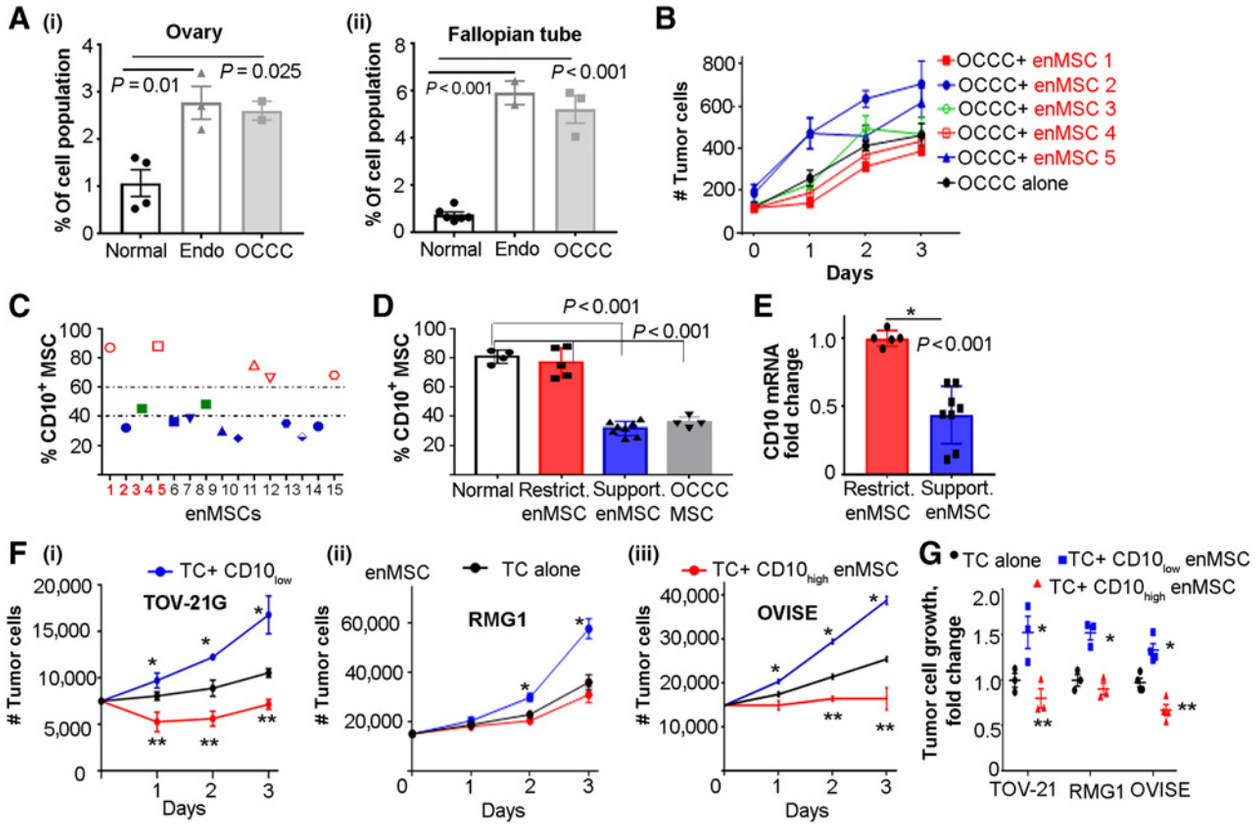

Figure 1.

Endometriosis contains MSCs and a subset of $CD10_{low}$ enMSCs support OCCC growth. **A,** Flow cytometric quantification of MSCs from normal ovary ($n = 4$), normal FT ($n = 6$), endometriosis ($n = 3$), or OCCC ($n = 3$) deposits in the ovary (i) and fallopian tube (ii). **B,** Fluorescently labeled OCCC cells were grown with different patient-derived enMSCs and OCCC cell numbers were counted over time, demonstrating enMSCs have variable impact on the proliferation of OCCC cells. **C,** Flow cytometric quantification of CD10 surface expression per patient sample demonstrating CD10 expression corresponds with OCCC growth promotion (blue symbols) or suppressive function (red symbols). Samples with intermediate CD10 expression did not impact OCCC growth (green symbols). enMSC sample numbers 1 to 5 (in red font) correspond with samples 1 to 5 (in red font) from **B**. **D**, Tumor supportive enMSCs (support. enMSC, $n = 8$) and patient-derived OCCC MSCs ($n = 4$) have significantly lower CD10 surface expression as measured via flow cytometry versus normal MSCs ($n = 4$) or tumor restrictive enMSC (restict. enMSC, $n = 5$). **E,** CD10 mRNA levels correspond to surface CD10 expression (compared for each patient sample). **F,** Quantification of OCCC cell numbers over time demonstrates $CD10_{low}$ enMSCs enhance OCCC growth in three OCCC cell lines and $CD10_{high}$ MSCs suppress OCCC growth in two OCCC cell lines. **G,** Change in 3-day TC growth, composite of three independent $CD10_{high}$ enMSC lines, three independent $CD10_{low}$ enMSC lines, and three OCCC lines. *, $P < 0.05$ $CD10_{low}$ enMSC vs. TC alone; **, $P < 0.05$ $CD10_{high}$ enMSC vs. TC alone. Mean and SEM are presented.

cell lines (TOV-21G, RMG1, OVISE; **Fig. 1F** and **G**). MSCs containing between 40% and 60% $CD10^+$ cells did not have a significant impact on OCCC growth. Importantly, presence or absence of CD10 expression, or intensity of CD10 staining did not impact the fundamental characteristics of MSCs with all lines meeting the ISCT criteria for MSCs, including marker expression, differentiation capacity, and baseline proliferation rates (Supplementary Fig. S1D).

To determine if the isolated enMSCs were derived from the ectopic endometrial stroma, which generated the endometriotic lesion or if they were derived from the underlying ovarian or fallopian tube tissue, we assessed the presence of markers reported to be expressed on endometrium-derived MSCs: CD146 and CD140b (23–25). Supplementary Fig. S2 demonstrates both the $CD10_{low}$ and $CD10_{high}$ enMSCs express surface levels of CD146 and CD140b, resembling the cell surface expression of primary endometrium-derived MSCs (obtained from human endometrium without pathology or endometriosis). In contrast, ovary and fallopian tube–derived MSCs and HGSC ovarian cancer derived CA-MSCs do not express cell surface CD146 and have substantially lower expression of CD140b. In addition, we assessed the impact of normal ovary and normal FT-derived MSCs on OCCC growth and found that neither MSC source altered OCCC growth (Supplementary Fig. S2B). Collectively, this supports an endometrial origin of the MSCs isolated from endometriotic tissue.

$CD10_{low}$ enMSCs selectively support OCCC growth

Given the unique microenvironment in which OCCC develops, we next sought to determine if $CD10_{low}$ enMSCs specifically enhance OCCC growth or if their protumorigenic impact is generalizable to other ovarian cancer histologic subtypes. Using a direct coculture system, we grew $CD10_{low}$ enMSCS with OCCC or HGSC ovarian cancer cells (OVSAHO and OVCAR3) and HGSC primary patient line pt412. As a comparator, we used CA-MSCs derived from primary patient HGSC ovarian cancer involving the ovary, which we previously demonstrated supports HGSC cell growth (9, 14, 26). $CD10_{low}$ enMSCs specifically enhanced the growth of OCCC while having no impact on HGSC cell growth (**Fig. 2A**). HGSC-derived CA-MSCs

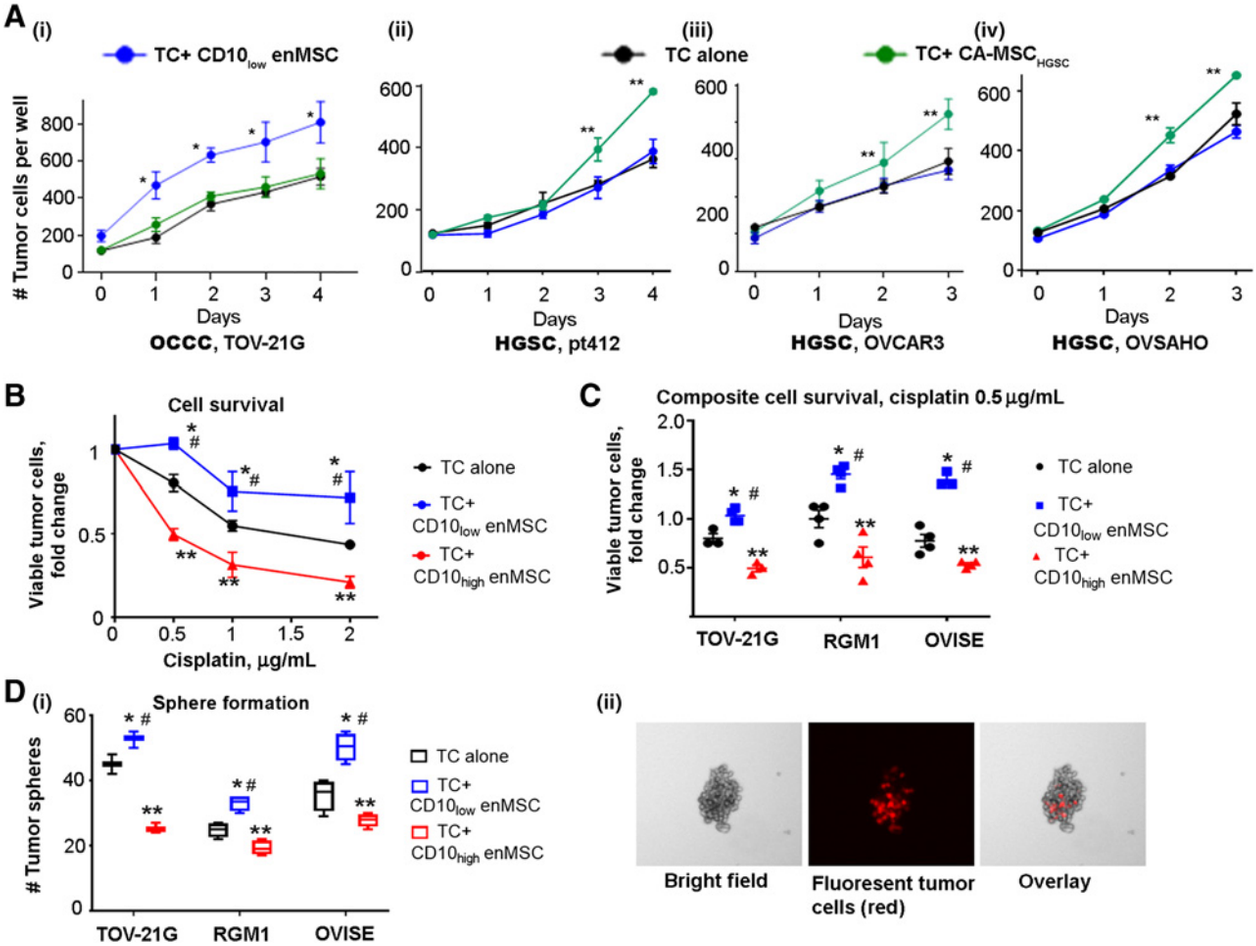

Figure 2.

$CD10_{low}$ enMSCs specifically support OCCC growth and do not impact HGSC growth. **A,** $CD10_{low}$ enMSCs or CA-MSCs derived from HGSC patient tissue ($CA\text{-}MSC_{HGSC}$) were grown with CellTrace Blue–labeled OCCC (i) or HGSC cells OVCAR3 (ii) and OVSAHO (iii) or primary patient derived HGSC cells pt412 (iv). The number of TCs quantified via cell counting demonstrated $CD10_{low}$ MSCs only enhance OCCC growth, whereas $CA\text{-}MSC_{HGSC}$ only support HGSC growth. *, $P < 0.05$ $CD10_{low}$ enMSCs vs. TC alone; **, $P < 0.05$ $CA\text{-}MSC_{HGSC}$ vs. TC alone. **B,** CellTrace Violet–labeled TCs (TOV-21G) grown alone or with $CD10_{low}$ enMSCs or $CD10_{high}$ enMSCs treated with cisplatin for 48 hours. Viable TCs were quantified, demonstrating $CD10_{low}$ enMSCs enhance TC chemotherapy resistance. Fold change vs. untreated control and SEM are plotted. **C,** Composite viable TCs (TOV-21G, RMG1, OVISE) grown alone or with enMSCs as in **B**. Fold change vs. untreated control is plotted with SEM. **D,** Fluorescently labeled TCs grown alone or with $CD10_{low}$ enMSCs or $CD10_{high}$ enMSCs under nonadherent conditions were assessed for sphere formation. The number of TC-containing spheres was quantified per group and demonstrate $CD10_{low}$ enMSCs enhance TC sphere growth. Average sphere number and SEM plotted. (ii) Representative picture of TC-containing sphere with both TC and enMSCs present. *, $P < 0.05$ $CD10_{low}$ enMSCs vs. TC alone; **, $P < 0.05$ $CD10_{high}$ enMSC vs. TC alone; #, $P < 0.05$ $CD10_{low}$ enMSC vs. $CD10_{high}$ enMSC.

increased HGSC cell growth while not impacting OCCC growth (**Fig. 2A**). This was repeated in additional OCCC lines, RMG1 and OVISE with similar results (Supplementary Figs. S3A and S3B). These provide further evidence that enMSCs from the endometriotic microenvironment are uniquely supportive of OCCC growth.

$CD10_{low}$ enMSCs support multiple aspects of OCCC growth

We expanded our investigation of the impact of enMSCs on OCCC growth by testing their effect on chemotherapy resistance and cancer cell sphere growth. $CD10_{low}$ enMSCs significantly enhanced the resistance of OCCC cells to cisplatin therapy. **Figure 2B** demonstrates the survival of OCCC TOV-21G cells cocultured with $CD10_{low}$ enMSCs or $CD10_{high}$ enMSCs when treated with increasing doses of cisplatin. The (fluorescently labeled) TC component of the coculture was quantified. Coculture with $CD10_{low}$ enMSCs significantly increased the survival of OCCC cells to cisplatin therapy. In contrast, the $CD10_{high}$ enMSCs decreased the survival of OCCCs cells to cisplatin therapy. We confirmed these results using three independent enMSC lines with two additional OCCC cell lines (OVISE and RMG1; **Fig. 2C**; Supplementary Figs. S3C and S3D). The same coculture experiments performed under nonadherent, spheroid-forming conditions also resulted in significantly more TC containing spheres with $CD10_{low}$ enMSCs. In contrast, $CD10_{high}$ enMSCs significantly decreased TC sphere formation (**Fig. 2D**).

$CD10_{low}$ enMSCs increase OCCC growth and metastasis *in vivo*

We next tested the impact of $CD10_{low}$ versus $CD10_{high}$ enMSCs on OCCC growth *in vivo*. We first used a subcutaneous model where TOV-21G cells with and without $CD10_{low}$ enMSCs or $CD10_{high}$ enMSCs were injected subcutaneously into mice. After 2 weeks,

$CD10_{low}$ enMSC containing tumors demonstrated increased tumor initiation with 90% engraftment versus 60% engraftment in the TOV-21G alone group and 40% engraftment in the $CD10_{high}$ enMSC containing tumors (**Fig. 3A**). In addition, the $CD10_{low}$ enMSC containing tumors also grew faster than the other two groups (**Fig. 3B**). Surprisingly, we also noted development of metastasis from the primary subcutaneous tumor with 60% of mice with $CD10_{low}$ enMSC containing tumors developing intra-abdominal metastasis and 80% developing lung metastasis. In comparison, 20% of mice with TOV-21G alone tumors developed abdominal metastasis related to direct extension of the tumor into the peritoneal cavity. In the $CD10_{high}$ enMSC containing tumor group, 20% of these mice developed lung metastasis (**Fig. 3C**).

To further evaluate the impact of enMSCs on OCCC growth, we used an orthotopic model where TOV-21G TCs with or without $CD10_{low}$ enMSCs or $CD10_{high}$ enMSCs were injected into the unilateral ovarian bursa as described previously (10, 12). TCs stably expressed luciferase and tumor engraftment, growth, and metastasis were monitored with IVIS bioluminescence imaging. Similar to the subcutaneous model, $CD10_{low}$ enMSC containing tumors initiated significantly faster than $CD10_{high}$ enMSC containing tumors or TCs alone. In addition, the $CD10_{low}$ enMSC containing tumors demonstrated faster growth and mice developed significantly more metastases compared with the other two groups (**Fig. 3D**). Ultimately, mice with $CD10_{low}$ enMSC containing tumors demonstrated decreased survival compared with mice with $CD10_{high}$ enMSC containing tumors (**Fig. 3E**). At the time of necropsy, we isolated both primary and metastatic tumors and assessed the presence and proportion of enMSCs at each site using flow cytometry. Both primary and metastatic tumors contained human enMSCs ranging from 0.2% to 5% of viable cells within the tumor. This is consistent with our previous work in HGSC demonstrating MSCs travel with cancer cells to metastatic sites (10). We quantified the frequency of $CD10^+$ cells among all tumor-isolated enMSCs from the initial $CD10_{low}$ enMSC and $CD10_{high}$ enMSC tumor groups. Interestingly, although the initial $CD10_{low}$ enMSC group (28% with CD10 surface expression) continued to demonstrate a low proportion of cells with surface CD10 expression at the end of the *in vivo* experiment (20.6% with CD10 surface expression, $P = 0.2$), the initial $CD10_{high}$ enMSC group (86% with CD10 surface expression) demonstrated a significant reduction in cells with CD10 surface expression at the end of the *in vivo* experiment (32% with CD10 surface expression, $P < 0.001$; **Fig. 3F**). These indicate there was either a selection for MSCs without CD10 expression in the tumors, which grew and metastasized, or TCs induced the reduction of CD10 expression in enMSCs *in vivo*.

OCCC stimulates the reduced expression of CD10 in enMSCs

We next sought to determine the mechanism of CD10 surface expression alterations in enMSCs. We first validated that enMSC CD10 surface expression also changes *in vitro* with cancer stimulation. We grew $CD10_{high}$ enMSCs with TOV-21G cells for 5 days. Consistent with our *in vivo* data, over time, the number of MSCs with CD10 surface expression decreased, changing from 69% positive to 14% positive by day 5 (**Fig. 4A**). We also tested which coculture conditions induced the greatest change in CD10 prevalence. We grew $CD10_{high}$ enMSCs with TOV-21G conditioned media versus indirect coculture with TOV-21G cells in a transwell system versus direct coculture with TOV-21G cells. After 5 days, the prevalence of CD10 surface expression on enMSCs was quantified with flow cytometry. Direct coculture was the most effective means of altering CD10 prevalence changing

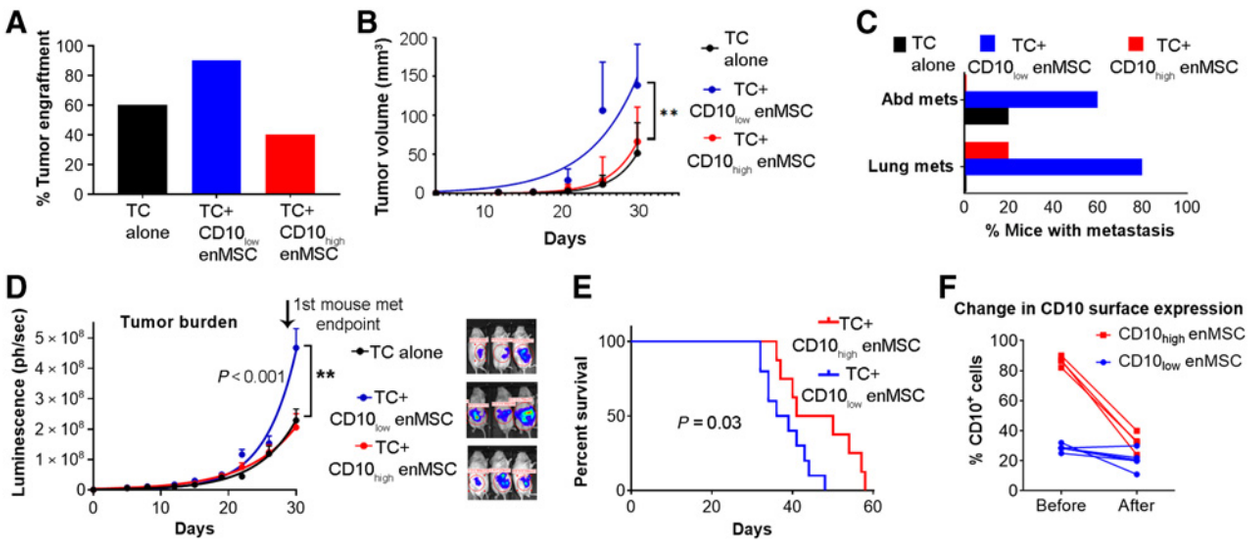

Figure 3.

$CD10_{low}$ enMSCs enhance the initiation, growth, and metastasis of OCCC cells in subcutaneous and orthotopic mouse models, leading to decreased mouse survival. **A,** TOV-21G TCs (TC) were injected alone or with $CD10_{low}$ enMSCs or $CD10_{high}$ enMSCs subcutaneously into NSG mice. Percent of mice with tumor engraftment per group is plotted, demonstrating $CD10_{low}$ enMSC containing tumors have increased engraftment. **B,** Volume of engrafted xenografts demonstrates increased tumor growth with $CD10_{low}$ enMSCs. **C,** Quantification of metastasis at time of necropsy demonstrated the $CD10_{low}$ enMSC group have increased metastatic burden. **D,** Luciferase-expressing TOV-21G TCs were injected alone or with $CD10_{low}$ enMSCs or $CD10_{high}$ enMSCs orthotopically into the unilateral ovarian bursa and tumor growth was measured via serial bioluminescence imaging, demonstrating increased growth in the $CD10_{low}$ enMSC containing tumors. **E,** Kaplan–Meier curve demonstrating mice with $CD10_{low}$ enMSC containing tumors had significantly decreased survival (log-rank test $P = 0.03$). **F,** enMSCs isolated from orthotopic xenografts at time of necropsy demonstrated stable surface expression of CD10 in the initial $CD10_{low}$ enMSCs but significant decrease in CD10 surface expression in the initial $CD10_{high}$ enMSCs. **, $P < 0.05$ $CD10_{low}$ enMSCs vs. TC alone.

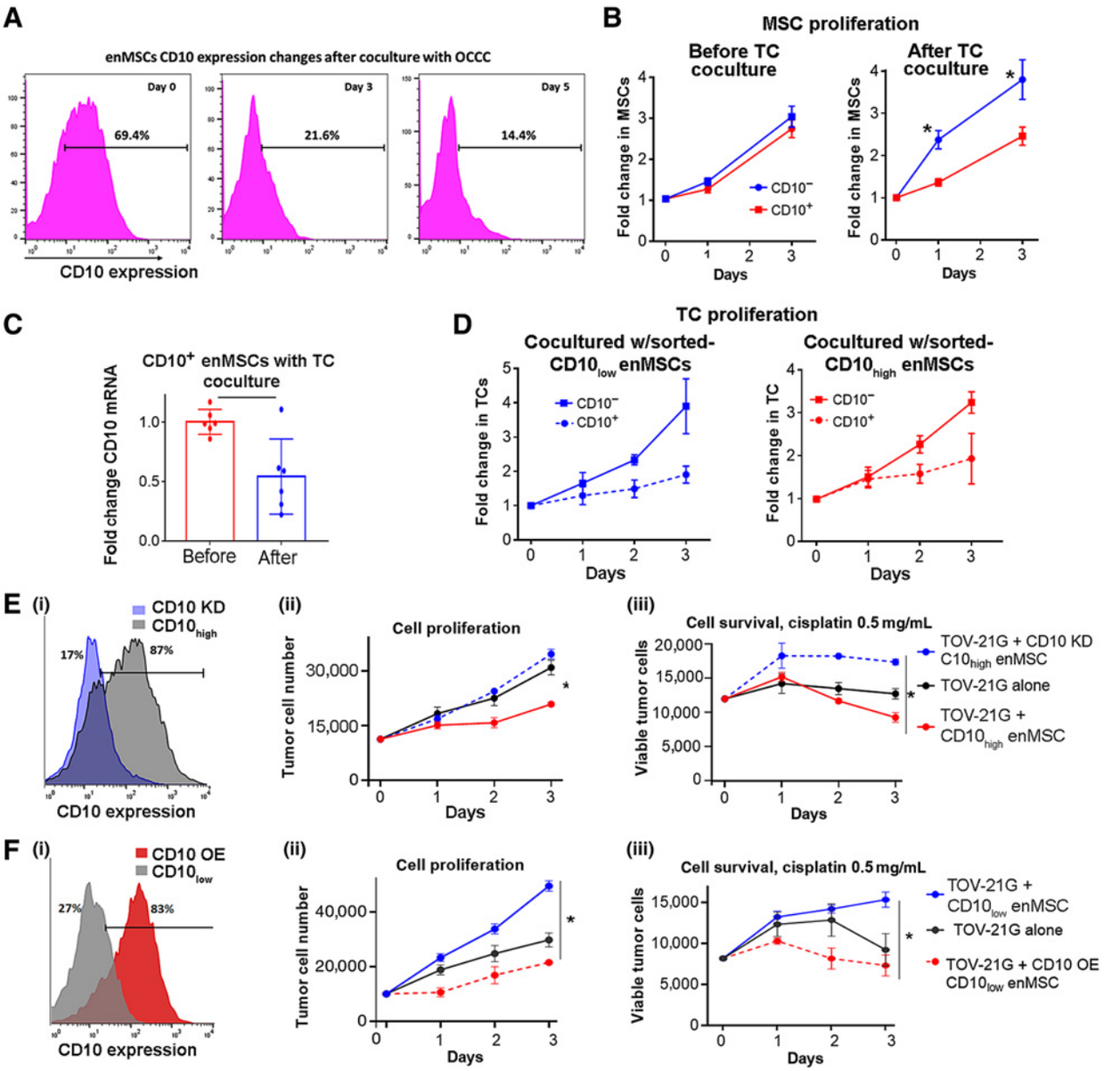

Figure 4.

OCCC decreases CD10 expression in enMSCs and loss of CD10 conveys protumorigenic functions. **A,** Flow cytometric quantification of CD10 surface expression in $CD10_{high}$ enMSCs before and after coculture with OCCC cells demonstrating decreased CD10 surface expression after coculture with TOV-21G cells. **B,** Quantification of cell numbers over time of sorted and fluorescently labeled $CD10^+$ vs. $CD10^-$ enMSCs demonstrated there is no significant difference in the baseline proliferation of $CD10^+$ vs. $CD10^-$ enMSCs. However, when grown in coculture with TCs, $CD10^-$ enMSCs have significantly increased proliferation vs. $CD10^+$ enMSCs. **C,** mRNA quantification of CD10 in the $CD10^+$ enMSCs before and after TC coculture (as performed in **B**). **D,** $CD10_{low}$ enMSCs (blue) and $CD10_{high}$ enMSCs (red) sorted into $CD10^-$ (solid lines) or $CD10^+$ (dashed lines) groups demonstrate TCs grown with $CD10^-$ enMSCs grow faster than TCs grown with $CD10^+$ enMSCs regardless of the initial group (CD10 high or low). **E,** (i) Lentiviral CD10 knockdown (KD) with shRNA of $CD10_{high}$ enMSCs results in 70% reduction in CD10 surface expression. CD10 KD prevents the $CD10_{high}$ enMSC-mediated growth inhibition of TOV-21G (ii) and enhances the survival of TOV-21G cells to cisplatin therapy (iii). **F**, (i) Lentiviral CD10 overexpression (OE) of $CD10_{low}$ enMSCs results in a 56% increase in CD10 surface expression. CD10 OE blocks the $CD10_{low}$ enMSC-mediated growth promotion of TOV-21G cells (ii) and prevents $CD10_{low}$ enMSC-mediated TOV-21G chemotherapy resistance (iii). *, $P < 0.05$ control enMSCs vs. KD or OE MSC. Mean and SEM are plotted.

from 90% $CD10^+$ enMSCs at baseline to 29% $CD10^+$ after coculture. The other experimental conditions had minimal effect on CD10 expression with 87.6% $CD10^+$ after 5 days of conditioned media and 84.3% $CD10^+$ after indirect coculture (Supplementary Fig. S4).

We next tested if differential growth rates between $CD10^-$ and $CD10^+$ enMSC lead to the altered proportion of CD10 expressing cells. We sorted enMSCs based on CD10 surface expression into $CD10^+$ and $CD10^-$ groups. We fluorescently labeled the $CD10^+$ cells with cell

trace blue and the CD10$^-$ cells with cell trace yellow to enable tracking and isolation of the original populations. We mixed the labeled CD10$^+$ and CD10$^-$ enMSCs in a 1:1 ratio. We quantified the proliferation of each population over time. There was no significant difference in the growth rate of the CD10$^+$ or CD10$^-$ enMSCs grown without cancer cells, demonstrating no inherent proliferation differences (**Fig. 4B**). We next directly cocultured the labeled CD10$^+$ and CD10$^-$ enMSCs with TOV-21G cells for 5 days (a time frame previously sufficient for HGSC cancer cells to educate MSCs; ref. 14). Surprisingly, when grown with cancer cells, the proliferation of the CD10$^-$ enMSCs increased ultimately growing faster than the CD10$^+$ population (**Fig. 4B**). Isolation of the initial CD10$^+$ enMSCs (fluorescently labeled to separate the initial CD10$^+$ population regardless of CD10 expression after coculture) also demonstrated decreases in CD10 mRNA after TC coculture (**Fig. 4C**). This is consistent with both decreased CD10 transcriptional expression in the CD10$^+$ population as well as increased proliferation of the CD10$^-$ enMSC population. These indicate that OCCC both induces the transcriptional downregulation of CD10 and selectively enhances the growth of CD10$^-$ enMSCs.

Loss of CD10 conveys protumorigenic functions

We next tested the functional significance of CD10 expression. We selected a $CD10_{low}$, cancer supportive enMSC sample and a $CD10_{high}$, cancer restrictive enMSC sample and sorted them into CD10$^+$ and CD10$^-$ populations. We then tested the impact of the CD10$^+$ versus CD10$^-$ enMSCs on OCCC growth. The CD10$^-$ subset derived from either the $CD10_{low}$ or $CD10_{high}$ parent cells significantly increased OCCC cancer growth compared with the CD10$^+$ subsets (from the $CD10_{low}$ or $CD10_{high}$ parent cells; **Fig. 4D**). Thus, the expression of CD10 rather than the phenotype of the parent cells drives the cancer supportive properties of enMSCs. Next, we created CD10 knockdown and CD10 overexpression enMSCs. We took the CD10$^+$ subset of a native $CD10_{high}$, nonsupportive enMSC sample and created stable CD10 knockdown (KD) via lentiviral shRNA. This resulted in a 5-fold reduction in CD10 surface expression compared with scrambled control parent enMSCs (**Fig. 4E**; Supplementary Fig. S5). CD10 KD enMSCs versus control parent enMSCs significantly enhanced the growth and chemotherapy resistance of OCCC (**Fig. 4E**). The impact of CD10 KD was validated in an additional, independent CD10$^+$ enMSC primary patient sample (Supplementary Fig. S5E).

We next overexpressed CD10 to determine if this would reverse the protumorigenic effects of the cancer supportive enMSCs. We used the CD10$^-$ population of a native $CD10_{low}$, cancer supportive enMSC sample. We then used a lentiviral CD10 construct to overexpress CD10, resulting in a 3-fold increase in surface expression of CD10 (**Fig. 4F**; Supplementary Fig. S5). CD10 overexpressed (OE) enMSCs versus scrambled control parent enMSCs lost the ability to support OCCC growth and chemotherapy resistance (**Fig. 4F**). The impact of CD10 OE was validated in an additional, independent CD10$^-$ enMSC primary patient sample (Supplementary Fig. S5F).

CD10$^-$ enMSCs have differential iron regulatory properties

To determine the difference between CD10$^+$ and CD10$^-$ enMSCs and to identify critical pathways that mediate their impact on OCCC growth, we performed RNA-seq on the CD10$^+$ population of $CD10_{high}$ enMSCs from 3 independent patients and the CD10$^-$ population of $CD10_{low}$ enMSCs from an additional 5 independent patients. To assess the impact on cancer cells, we also performed RNA-seq on TOV-21G cancer cells cocultured with CD10$^-$ enMSCs or CD10$^+$ enMSCs (four independent cocultured samples per group). **Figure 5** demonstrates the unsupervised hierarchical clustering of the CD10$^-$ versus CD10$^+$ enMSCs demonstrating clear separation by CD10 expression with distinct transcriptomic changes. A volcano plot of the most significantly DEGs demonstrates increased expression of 606 genes and decreased expression of 506 genes (**Fig. 5B, i**). Similarly, comparison of the cancer cells cocultured with CD10$^-$ versus CD10$^+$ enMSCs also demonstrated significant alterations in the transcriptome with 1,054 upregulated and 1,355 downregulated genes (**Fig. 5A, ii** and **B, ii**). Top DEGs were validated using qRT-PCR in independent enMSC and cocultured TC samples. Pathway analysis highlighted changes in metal/ion transport and regulation as the top differentially regulated pathways in cancer cells grown with CD10$^+$ versus CD10$^-$ enMSCs (**Fig. 5D**). In additiojn, a gene associated with protection against ferroptosis (iron-mediated cell death), ribonucleotide reductase regulatory subunit M 2 (*RRM2*), was significantly overexpressed in TCs grown with CD10$^-$ enMSCs (**Fig. 5C, ii**; ref. 27). In line with this, Hephaestin (*HEPH*) was one of the top genes significantly overexpressed in the CD10- enMSC population. Hephaestin is a ferroxidase critical to iron export (28). Hephaestin converts Fe^{2+} to Fe^{3+} enabling iron to be transported out of the cell by ferroportin (FPN1; ref. 29).

Given alterations in metal transport and handling in OCCC grown with CD10$^-$ enMSCs and the upregulation of *HEPH* in the CD10$^-$ enMSCs, we investigated iron regulation in the TME as a potential mechanism of CD10$^-$ enMSC-mediated OCCC growth promotion.

CD10$^-$ enMSCs increase OCCC intracellular iron levels through iron export into the TME

We hypothesized that increased HEPH in the CD10$^-$ enMSCs results in iron export, which increases iron in the extracellular TME for use by OCCC cells to support growth. Iron is critical to cancer cell growth, and OCCC may have unique requirements for iron given its association with hypoxia and endometriosis (6, 30, 31). We first investigated the expression of iron regulatory genes in enMSCs. We validated increased protein levels of HEPH in CD10$^-$ versus CD10$^+$ enMSCs via Western blot analysis (**Fig. 6A** and **B**). Consistent with increased iron export capacity, we also demonstrated increased FPN1 in CD10$^-$ versus CD10$^+$ enMSCs (**Fig. 6A** and **B**).

We also demonstrated significantly increased levels of the iron storage protein, ferritin (FT), in CD10$^-$ versus CD10$^+$ enMSCs. FT is composed of two subunits, ferritin H (FTH) and ferritin L (FTL). FTH is the subunit with ferroxidase activity necessary to store iron within the ferritin complex whereas FTL is the main storage subunit (32). The levels of FTH were not significantly different whereas levels of FTL were increased 2-fold in CD10$^-$ versus CD10$^+$ enMSCs. Interestingly, when we evaluated TCs with and without coculture with CD10$^-$ versus CD10$^+$ enMSCs, we identified a significant shift in the ratio of FTH versus FTL. Coculture of TCs with CD10$^-$ enMSCs resulted in a 2.6-fold increase in FTL but −2.5-fold decrease in FTH. Coculture with CD10$^+$ enMSCs demonstrated nonsignificant changes in FTH and FTL. We then quantified the levels of transferrin receptor (TFR; the main mechanism of cellular iron uptake; ref. 33) in OCCCs with and without coculture with CD10$^-$ and CD10$^+$ enMSCs. Interestingly, coculture with CD10$^-$ and CD10$^+$ enMSCs led to an increase in TC TFR compared with TCs grown alone. As FT and TFR are canonically inversely related via posttranslational regulation based on intracellular iron stores, this finding was unexpected (34). To more definitively assess levels of intracellular iron, we next measured the LIP (the amount of free or accessible iron within the cell) in CD10$^-$ versus CD10$^+$ enMSCs and in TOV-21G cells before and after coculture with enMSCs. The TOV-21G LIP is strikingly increased (2.2-fold increase) after coculture with CD10$^-$ enMSCs and decreased after coculture

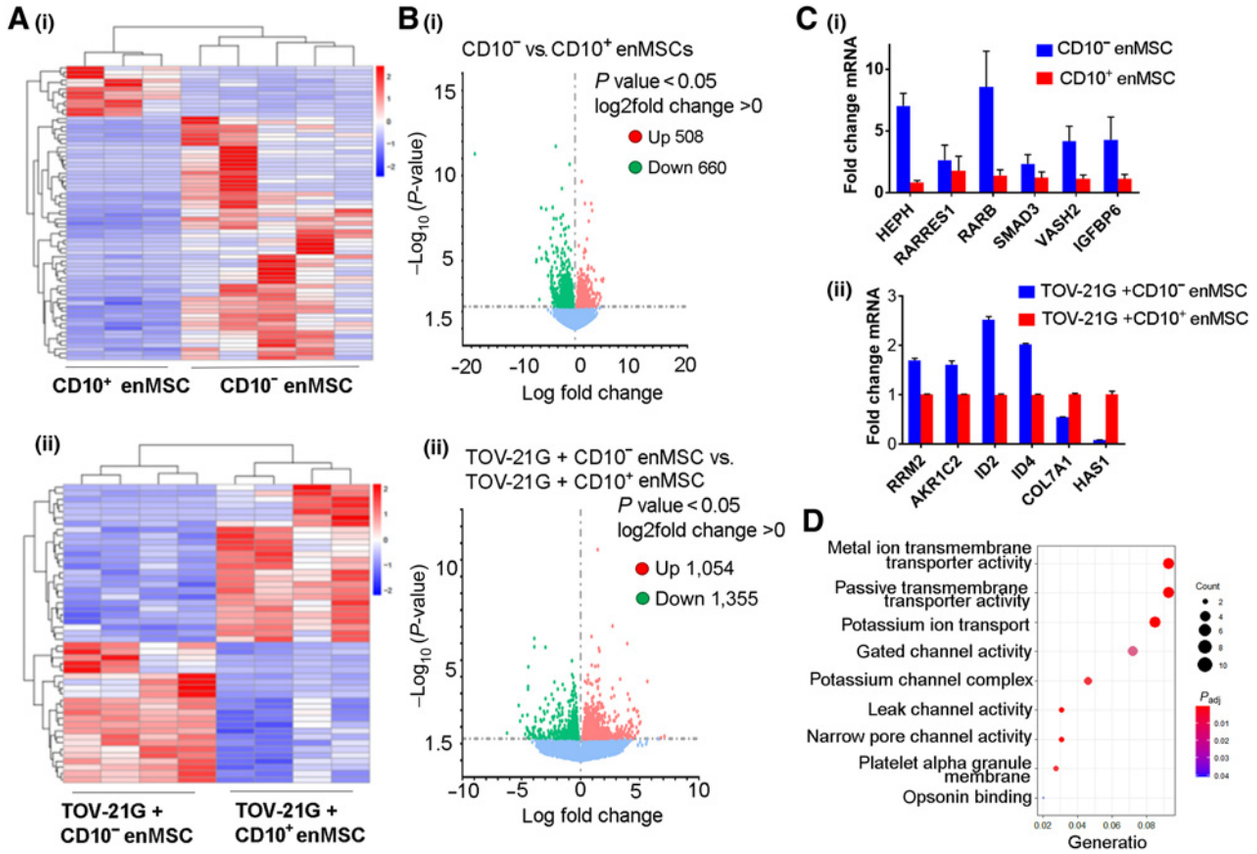

Figure 5.

RNA-seq demonstrates differential iron regulatory pathways in CD10$^+$ vs. CD10$^-$ enMSCs and metal/ion transport pathways in cocultured TOV-21G cells. **A,** Heatmap of unsupervised hierarchical clustering of CD10$^-$ vs. CD10$^+$ enMSCs (i) and TOV-21G cells grown with CD10$^-$ vs. CD10+ enMSCs (ii). **B,** Volcano plots demonstrating DEGs in CD10$^-$ vs. CD10$^+$ enMSCs (i) and TOV-21G cells (ii) grown with CD10$^-$ vs. CD10$^+$ enMSCs. **C,** Validation of top DEGs. **D,** Pathway analysis of DEG highlighting differences in metal transport and iron regulation.

with CD10$^+$ enMSC with a −3-fold decrease in LIP (**Fig. 6C**). CD10$^-$ enMSC have a baseline higher LIP compared with CD10$^+$ enMSCs and there is a proportional decrease in the LIP of CD10$^-$ enMSCs after coculture with TOV-21G cells, which corresponds to the rise in LIP of TOV-21G cells (**Fig. 6D**). This provides evidence that CD10$^-$ enMSCs donate iron to OCCC cells.

To further test this hypothesis, we used the iron chelator, deferoxamine (DFO; **Fig. 6E**). We treated OCCC cells grown alone or with CD10$^-$ versus CD10$^+$ enMSCs with increasing doses of DFO. DFO was added to standard serum-supplemented media, which contains iron and transferrin. Chelation of iron with DFO decreased the proliferation of OCCC cells grown alone, demonstrating the necessity of iron for OCCC growth (**Fig. 6E**). At low levels of DFO, CD10$^-$ enMSCs were able to rescue OCCC cells from the growth inhibiting effects of DFO, consistent with donation of iron by CD10$^-$ enMSCs. However, increased doses of DFO blocked CD10$^-$ enMSC-mediated OCCC growth promotion, indicating high levels of iron chelation can overcome the effects of CD10$^-$ enMSCs. This was not due to toxicity of DFO on the enMSC population. Collectively, this indicates CD10$^-$ enMSCs support OCCC growth through enhancing intracellular iron.

To test if increased extracellular iron alone (without the presence of enMSCs) alters OCCC growth, we added increasing doses of FAC (0.05–0.2 μmol/L) to TOV-21G cells grown alone in standard serum-supplemented media and measured proliferation over time. Interestingly, FAC did not significantly enhance the proliferation of OCCC and at higher levels it proved toxic. We concurrently assessed the changes in canonical iron import and storage proteins (TFR, FTL, and FTH) and the LIP. FAC treatment decreased TFR and increased FTL and FTH with no significant change in the LIP consistent with expected canonical regulation of iron storage proteins and maintenance of a stable LIP (Supplementary Fig. S6).

CD10$^-$ enMSCs sensitize OCCC cells to ferroptosis *in vitro* and *in vivo*

The above data indicates CD10$^-$ enMSCs enhance OCCC growth at least in part through increasing the LIP. However, labile intracellular iron can be toxic, leading to increased reactive oxygen species, lipid peroxidation, and ferroptosis. Indeed, as demonstrated above, OCCC cells grown with CD10$^-$ enMSCs upregulate *RRM2*, which is a ferroptosis-responsive gene. On the basis of this, we hypothesized that CD10$^-$ enMSCs induce a unique susceptibility of OCCC to ferroptosis. To test this, we treated OCCC cells alone or with CD10$^-$ versus CD10$^+$ enMSCs with the ferroptosis inducer, erastin (35). Erastin, even at doses as low as 0.5 μmol/L, significantly decreased

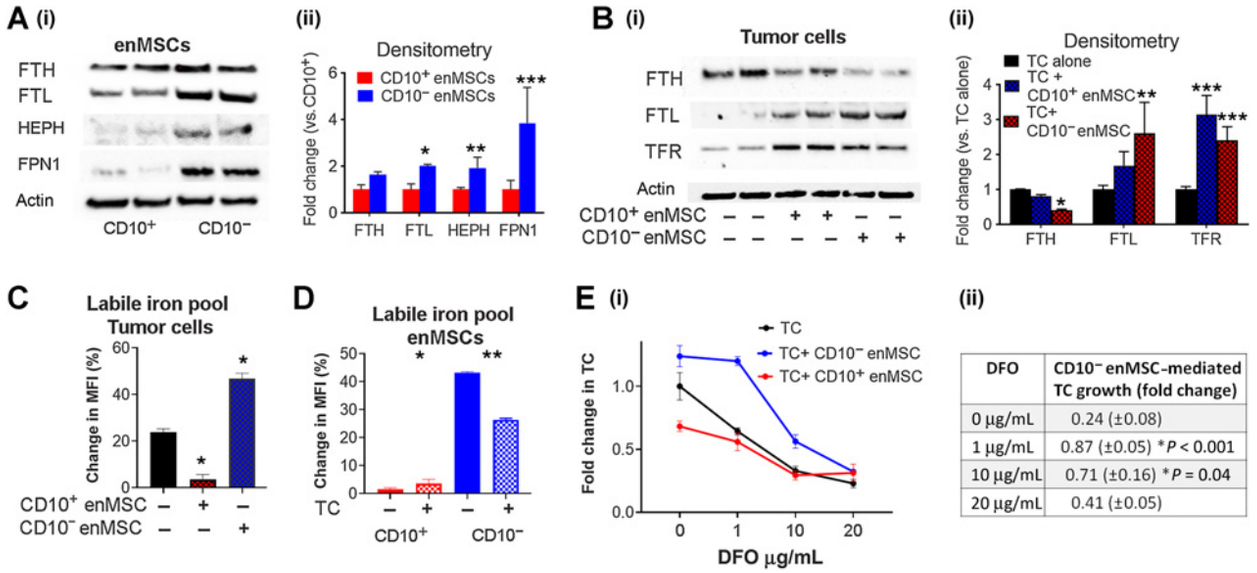

DFO	CD10⁻ enMSC–mediated TC growth (fold change)
0 µg/mL	0.24 (±0.08)
1 µg/mL	0.87 (±0.05) *P < 0.001
10 µg/mL	0.71 (±0.16) *P = 0.04
20 µg/mL	0.41 (±0.05)

Figure 6.

CD10⁻ enMSCs increase intracellular iron in OCCC cells. **A,** Western blot (i) and densitometry-based quantification (ii) of ferritin H and L subunits (FTH, FTL), hephaestin (HEPH), and FPN1 in CD10⁺ vs. CD10⁻ enMSCs, demonstrating increased iron storage and iron export proteins in CD10⁻ enMSCs. **B,** Western blot (i) and densitometry-based quantification (ii) of FTH, FTL, and transferrin receptor (TFR) in OCCC alone or cocultured with CD10⁻ or CD10⁺ enMSCs demonstrating altered FTH to FTL ratios and increased TFR after coculture with CD10⁻ enMSCs. **C,** Measurement of the LIP in TCs grown with CD10⁻ or CD10⁺ enMSCs, demonstrating increased LIP after CD10⁻ enMSC coculture. **D,** Measurement of the LIP in enMSCs before and after coculture with TCs, demonstrating decreased LIP in the CD10⁻ enMSCs after coculture. **E,** Proliferation of TCs grown with CD10⁻ enMSCs, CD10⁺ enMSCs or alone treated with increasing doses of the iron chelator, DFO (i). (ii) Quantification of CD10⁻ enMSC TC growth promotion with increasing doses of DFO. *, **, ***, $P < 0.05$.

the number of OCCC cells grown with CD10⁻ enMSCs whereas only the highest dose of erastin (10 µmol/L) significantly decreased the numbers of OCCC cells grown alone. CD10⁺ enMSCs provided protection against erastin at the 10 µmol/L dose (**Fig. 7A**). The IC_{50} of erastin in OCCC cells (TOV-21G) alone was 7.2 µmol/L versus 1.1 µmol/L in OCCC cells + CD10⁻ enMSCs. We repeated these experiments with another ferroptosis inducer, DHA (36). DHA treatment resulted in a 2- to 3-fold increase in OCCC cell death when grown with CD10⁻ enMSCs (IC_{50} 1.2 µmol/L) versus OCCC cells grown alone (IC_{50} 5.1 µmol/L) or with CD10⁺ enMSCs (IC_{50} 9.5 µmol/L) consistent with CD10⁻ enMSC enhancing the sensitivity of OCCC cells to ferroptosis (**Fig. 7B**).

To verify the induction of ferroptosis, we performed BoDIPY 581/591 C11 staining followed by flow cytometry to detect lipid peroxidation, which is a hallmark of ferroptosis (21). After treatment with 1 µmol/L erastin, OCCC cells grown with CD10⁻ enMSC demonstrated significantly more lipid peroxidation compared with OCCCs grown alone or with CD10⁺ enMSCs consistent with increased induction of ferroptosis (**Fig. 7C**). We also performed immunofluorescence to detect 4-HNE, which is a derivative of lipid peroxidation (37). Consistent with the BoDIPY analysis, 4-HNE staining was significantly increased in OCCCs with CD10⁻ enMSC versus OCCCs alone or OCCCs with CD10⁺ enMSCs treated with low doses of erastin (1 µmol/L; **Fig. 7D**).

We then performed an *in vivo* study with TOV-21G cells with CD10⁻ versus CD10⁺ enMSCs injected into the ovarian bursa of NSG mice. TCs were luciferase labeled. Tumors were allowed to engraft for 5 days. Low-dose erastin treatment (10 mg/kg daily) or vehicle control was started on day 5 and continued daily for 20 days. Tumor burden was followed with IVIS imaging and mice were followed for survival. Erastin significantly decreased tumor growth and improved the survival of mice with CD10⁻ enMSC containing tumors (**Fig. 7E** and **F**). Mice with CD10⁻ enMSC containing tumors treated with erastin had equivalent survival to mice with CD10⁺ enMSC containing tumors (**Fig. 7F**). This indicates erastin reversed the protumorigenic impact of CD10⁻ enMSCs and ultimately turned the growth promoting effects of iron donation into a therapeutic liability significantly sensitizing OCCC cells to ferroptosis. At time of sacrifice, we resected tumors and verified enMSCs were present in all groups at both the primary and metastatic sites. We also compared the CD10 surface expression of isolated enMSCs from the CD10⁻ groups. Interestingly, the CD10 expression on enMSCs increased with erastin treatment compared with control treatment (**Fig 7**G). Thus, erastin both induced ferroptosis in TCs grown with CD10⁻ enMSCs and altered the CD10 expression on enMSCs, resulting in a higher proportion of CD10⁺ enMSCs, both of which may contribute to the overall survival benefit of erastin treatment.

Discussion

Here we identify a novel subset of enMSCs that selectively support OCCC growth. These OCCC-supportive enMSCs are marked by decreased CD10 expression. This subset of CD10⁻ enMSCs have increased iron export proteins, resulting in reciprocal increases of intracellular iron within OCCC cells. Thus, iron regulation is a critical mechanism driving CD10⁻ enMSC support of OCCC growth. Importantly, this also implies a unique therapeutic vulnerability as CD10⁻ enMSC increase the susceptibility of OCCC to the ferroptosis inducers erastin and DHA. Therefore, the growth promoting effects of CD10⁻ enMSCs can be weaponized to kill OCCC.

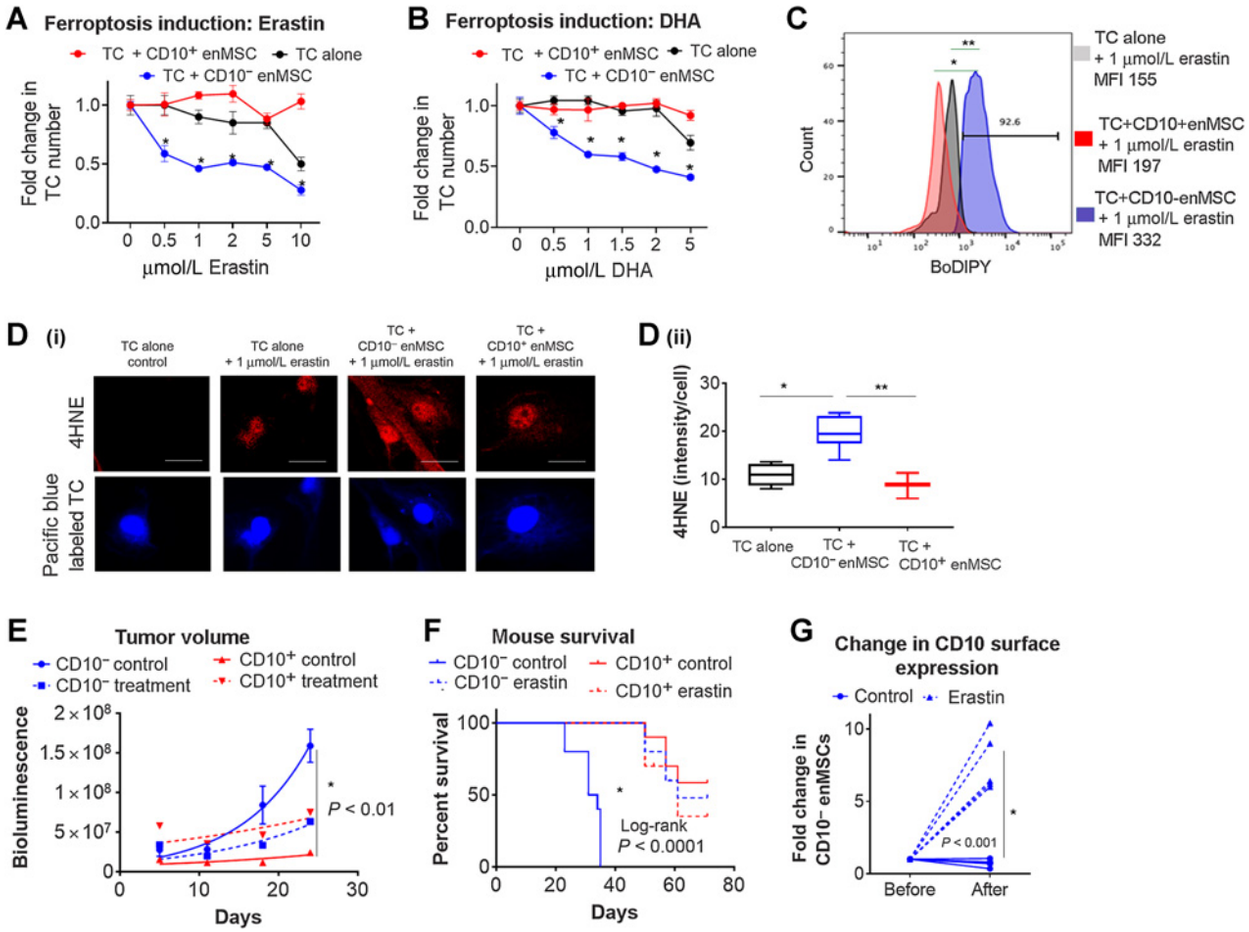

Figure 7.

CD10- enMSCs sensitize OCCC to ferroptosis. **A,** *In vitro* dose response curve with erastin. Viable OCCC tumors cells (TC) with and without CD10+ vs. CD10- enMSCs were quantified and are represented as fold change from no treatment control. **B,** *In vitro* dose response curve with DHA (assessed as in **A**). **C,** BoDIPY stain quantifying lipid peroxidation in TC with and without CD10+ vs. CD10- enMSCs treated with 1 µmol/L erastin. *, $P < 0.05$ TC+CD10-enMSC vs. TC+CD10+ enMSC; **, $P < 0.05$ TC+CD10- enMSC vs. TC alone. **D,** 4-HNE staining of OCCC with and without CD10+ vs. CD10- enMSCs treated with 1 µmol/L erastin. TC was labeled with Pacific Blue. Representative immunofluorescence images (i). Scale bar, 25 µm. Quantification of fluorescent signal per cell (5 independent fields of view per condition; ii). *, $P < 0.05$ erastin-treated TC alone vs. TC^+CD10^- enMSC; **, $P < 0.05$ erastin-treated TC^+CD10^- enMSC vs. TC^+CD10^+ enMSC. **E** and **F,** *In vivo* tumor burden measured via IVIS imaging (**E**) and survival of mice with $CD10^+$ vs. $CD10^-$ enMSC containing tumors treated with and without erastin (**F**). **G,** Change in CD10 surface expression in $CD10^-$ enMSCs grown with TCs *in vivo* with control vs. erastin treatment.

Endometriosis-derived stromal support of OCCC

Our work further links the specific endometriotic microenvironment with OCCC growth and supports the unique role of endometriosis-derived stromal cells in the pathophysiology of OCCC. It is intriguing that $CD10^-$ enMSCs support OCCC but not HGSC, further highlighting the specificity of unique microenvironments for selective cancer growth. These findings also emphasize the fundamental differences in ovarian cancer histologic subtypes, underlining the need to study each subtype independently. It should be noted that we used the TOV-21G cell line as our main OCCC model, however results were repeated and confirmed in RMG1 and OVISE cell lines. Although RMG1 and OVISE are largely considered representative of clear cell histology, they lack some classic clear cell features (RMG1 lacks ARID1a mutation) and this may be why, in some experiments, the impact of $CD10^-$ enMSCs are more pronounced in the TOV-21G line (38, 39).

OCCC alters CD10 expression and the stromal phenotype

It is also interesting that not all endometriosis derived MSCs support OCCC growth. Identification of CD10 loss as a marker of MSCs with cancer supportive properties points to both a potential biomarker of "at risk" endometriosis tissue and begins to identify potential mechanisms for the stromal support of OCCC. We also demonstrate that OCCC acts upon enMSCs to induce a protumorigenic phenotype. OCCC cells alter the proportion of $CD10^+$ versus $CD10^-$ enMSCs, thus converting a baseline $CD10_{high}$ enMSC population into a $CD10_{low}$ enMSC population. This corresponds with the acquisition of OCCC supportive properties. Indeed, our *in vitro* work demonstrated $CD10_{high}$ enMSCs restrict OCCC growth, however this was not pronounced *in vivo*. Upon further evaluation, after *in vivo* growth with OCCC, the initial $CD10_{high}$ enMSC population demonstrated a significant decrease in CD10 expression such that only 20% to 30% of enMSC continued to express CD10. The loss of CD10

expression likely altered the phenotype of the enMSC, thus leading to growth promotion rather than suppression. CD10 OE and KD experiments confirmed the functional importance of CD10, however it is possible that other cell features, intrinsic to the enMSC or as a result of CD10 expression, also contribute to the impact of enMSCs on OCCC. Further work is necessary to delineate the full impact of CD10 on enMSC function.

The ability of OCCC cells to alter the surrounding stromal population to enhance the prevalence of the $CD10^-$ subset of MSCs is similar to our findings in HGSC, where cancer cells convert normal MSCs into cancer supportive CA-MSCs. We demonstrate that OCCC cells induce a selective growth advantage of the $CD10^-$ enMSC population but also transcriptionally downregulate CD10 expression in $CD10^+$ enMSCs. We also demonstrate direct coculture of enMSCs with OCCCs is the most effective means of CD10 loss implying direct cell interactions mediate the alterations in CD10. The mechanism underlying these alterations has yet to be discovered and will be the focus of future work. However, it is clear that the loss of CD10 expression is functionally important conveying protumorigenic properties to enMSCs.

$CD10^-$ enMSC alter iron regulation to enhance OCCC growth

The identification of altered iron regulation mediating the stromal support of OCCC is critically important. Although the mechanism governing total body iron homeostasis is well-defined, very little is known regarding the handling of iron within the tumor microenvironment. This may be of particular importance in the endometriosis microenvironment given the accumulation of iron due to continued menstrual cycling and thus the handling of iron may be vital to the prevention or development of OCCC. Here we present a new paradigm with $CD10^-$ enMSCs donating iron to OCCC to mediate cancer cell growth. Interestingly, the donated iron appears to remain in the LIP rather than sequestered in ferritin. This may be due to the altered FTH versus FTL ratio with a relative decrease in FTH, which is the subunit necessary for iron oxidation to enable iron storage. The finding that increasing extracellular iron alone is insufficient to enhance the OCCC LIP and cell proliferation further supports the importance of $CD10^-$ enMSC alteration of TC iron handling. OCCC cells respond to increased extracellular iron alone (without the presence of $CD10^-$ enMSCs) with canonical increases in both FTL and FTH, decreased TFR and maintenance of a stable LIP without appreciable change in cell proliferation. This indicates that not only are the $CD10^-$ enMSCs exporting iron, they are also altering iron handling within the TC, which ultimately increases the LIP and cell proliferation.

Therapeutic potential of ferroptosis induction with $CD10^-$ stroma

This increase in labile iron appears necessary for enMSC-mediated OCCC growth, however this leaves the OCCC cells susceptible to ferroptosis. Indeed, decreased FTH is associated with ferroptosis (40). Even relatively low doses of ferroptosis inducers, erastin or DHA, significantly decreased the survival of OCCC cells grown with $CD10^-$ enMSCs *in vitro* with an IC_{50} of 1.1 and 1.2 μmol/L respectively (compared with 7.2 and 5.1 μmol/L with OCCC cells alone). Other groups have investigated the cytotoxicity of ferroptosis inducers in cancer cells potentially susceptible to ferroptosis such as gastric cancer (erastin IC_{50} of 14 μmol/L; ref. 41) and hepatocellular cancer (DHA IC_{50} values of 20–40 μmol/L; ref. 42). More importantly, ferroptosis induction in the presence of $CD10^-$ enMSCs lead to dramatic decreases in tumor growth and increases in mouse survival *in vivo*. Importantly, the majority of MSCs associated with OCCC (100% of the cases we have sampled, **Fig. 1D**) are $CD10_{low}$ thus ferroptosis inducers represent a promising therapeutic avenue for OCCC. Importantly, *in vivo* erastin treatment also impacted the phenotype of the enMSCs increasing the proportion of $CD10^+$ enMSCs. This indicates inducing ferroptosis may have a dual effect of both enhancing TC death and altering the protumorigenic stroma thus magnifying the potential therapeutic benefit.

In addition, the loss of CD10 stromal expression may mark endometriosis tissue at risk for malignant transformation and may have important implications for risk stratification and prevention strategies. Future work is needed to explore the relationship between CD10 stromal loss and malignant transformation within the endometriotic microenvironment.

Collectively, this work provides novel insights into the stromal support of OCCC growth, and specifically identifies stromal-mediated iron regulation within endometriosis as an important driver of OCCC biology. This work also demonstrates the potential to capitalize on stromal-mediated iron regulation to increase OCCC susceptibility to ferroptosis.

Authors' Disclosures

A.M. Vlad reports grants from UPMC during the conduct of the study; grants from NIH, Merck, OCRA, and DOD-OCRP outside the submitted work; and also has a patent for Application 16/798,137 pending. L.G. Coffman reports grants from The Brenda and Roger Gibson Clear-Cell Cancer Research Fund during the conduct of the study and other support from Immunogen outside the submitted work. No disclosures were reported by the other authors.

Authors' Contributions

H.I. Atiya: Conceptualization, formal analysis, investigation, writing–original draft, writing–review and editing. **L. Frisbie:** Formal analysis, investigation, writing–review and editing. **E. Goldfeld:** Investigation, writing–review and editing. **T. Orellana:** Investigation, writing–review and editing. **N. Donellan:** Resources, investigation, methodology. **F. Modugno:** Resources, methodology. **M. Calderon:** Investigation, writing–review and editing. **S. Watkins:** Investigation, writing–review and editing. **R. Zhang:** Conceptualization, investigation, writing–review and editing. **E. Elishaev:** Resources, investigation. **T.R. Soong:** Formal analysis, investigation, writing–review and editing. **A. Vlad:** Resources, methodology, writing–review and editing. **L. Coffman:** Conceptualization, resources, data curation, formal analysis, supervision, funding acquisition, investigation, methodology, writing–original draft, project administration, writing–review and editing.

Acknowledgments

L.G. Coffman was supported by the Brenda and Roger Gibson Clear-Cell Cancer Research Fund and grant K08CA211362-04. H.I. Atiya was supported by The HERA Ovarian Cancer Foundation Outside the Box Research Grant.

The publication costs of this article were defrayed in part by the payment of publication fees. Therefore, and solely to indicate this fact, this article is hereby marked "advertisement" in accordance with 18 USC section 1734.

Note

Supplementary data for this article are available at Cancer Research Online (http://cancerres.aacrjournals.org/).

Received April 19, 2022; revised August 31, 2022; accepted October 7, 2022; published first October 11, 2022.

References

1. Siegel RL, Miller KD, Jemal A. Cancer statistics, 2016. CA Cancer J Clin 2016;66:7–30.
2. Lee YY, Kim TJ, Kim MJ, Kim HJ, Song T, Kim MK, et al. Prognosis of ovarian clear cell carcinoma compared to other histological subtypes: a meta-analysis. Gynecol Oncol 2011;122:541–7.
3. Mabuchi S, Sugiyama T, Kimura T. Clear cell carcinoma of the ovary: molecular insights and future therapeutic perspectives. J Gynecol Oncol 2016;27:e31.
4. Samartzis EP, Labidi-Galy SI, Moschetta M, Uccello M, Kalaitzopoulos DR, Perez-Fidalgo JA, et al. Endometriosis-associated ovarian carcinomas: insights into pathogenesis, diagnostics, and therapeutic targets—a narrative review. Ann Transl Med 2020;8:1712.
5. Hermens M, van Altena AM, Nieboer TE, Schoot BC, van Vliet HAAM, Siebers AG, et al. Incidence of endometrioid and clear-cell ovarian cancer in histological proven endometriosis: the ENOCA population-based cohort study. Am J Obstet Gynecol 2020;223:107.
6. Kobayashi H, Yamada Y, Kanayama S, Furukawa N, Noguchi T, Haruta S, et al. The role of iron in the pathogenesis of endometriosis. Gynecol Endocrinol 2009;25:39–52.
7. Wen CP, Lee JH, Tai YP, Wen C, Wu SB, Tsai MK, et al. High serum iron is associated with increased cancer risk. Cancer Res 2014;74:6589–97.
8. Coussens LM, Werb Z. Inflammation and cancer. Nature 2002;420:860–7.
9. McLean K, Gong Y, Choi Y, Deng N, Yang K, Bai S, et al. Human ovarian carcinoma-associated mesenchymal stem cells regulate cancer stem cells and tumorigenesis via altered BMP production. J Clin Invest 2011;121:3206–19.
10. Fan H, Atiya HI, Wang Y, Pisanic TR, Wang TH, Shih IM, et al. Epigenomic reprogramming toward mesenchymal-epithelial transition in ovarian-cancer-associated mesenchymal stem cells drives metastasis. Cell Rep 2020;33:108473.
11. Kao AP, Wang KH, Chang CC, Lee JN, Long CY, Chen HS, et al. Comparative study of human eutopic and ectopic endometrial mesenchymal stem cells and the development of an in vivo endometriotic invasion model. Fertil Steril 2011;95:1308–15.
12. Atiya HI, Orellana TJ, Wield A, Frisbie L, Coffman LG. An orthotopic mouse model of ovarian cancer using human stroma to promote metastasis. J Vis Exp 2021.
13. Dominici M, Le Blanc K, Mueller I, Slaper-Cortenbach I, Marini F, Krause D, et al. Minimal criteria for defining multipotent mesenchymal stromal cells. The International Society for Cellular Therapy position statement. Cytotherapy 2006;8:315–7.
14. Coffman LG, Pearson AT, Frisbie LG, Freeman Z, Christie E, Bowtell DD, et al. Ovarian Carcinoma-associated mesenchymal stem cells arise from tissue-specific normal stroma. Stem Cells. 2019;37:257–69.
15. Kim D, Langmead B, Salzberg SL. HISAT: a fast spliced aligner with low memory requirements. Nat Methods 2015;12:357–60.
16. Liao Y, Smyth GK, Shi W. featureCounts: an efficient general purpose program for assigning sequence reads to genomic features. Bioinformatics 2014;30:923–30.
17. Love MI, Huber W, Anders S. Moderated estimation of fold change and dispersion for RNA-seq data with DESeq2. Genome Biol 2014;15:550.
18. Wu T, Hu E, Xu S, Chen M, Guo P, Dai Z, et al. clusterProfiler 4.0: A universal enrichment tool for interpreting omics data. Innovation (N Y). 2021;2:100141.
19. Supek F, Bosnjak M, Skunca N, Smuc T. REVIGO summarizes and visualizes long lists of gene ontology terms. PLoS One 2011;6:e21800.
20. Prus E, Fibach E. Flow cytometry measurement of the labile iron pool in human hematopoietic cells. Cytometry A 2008;73:22–7.
21. Martinez AM, Kim A, Yang WS. Detection of Ferroptosis by BODIPY™ 581/591 C11. Methods Mol Biol 2020;2108:125–30.
22. Toki T, Shimizu M, Takagi Y, Ashida T, Konishi I. CD10 is a marker for normal and neoplastic endometrial stromal cells. Int J Gynecol Pathol 2002;21:41–7.
23. Schwab KE, Gargett CE. Co-expression of two perivascular cell markers isolates mesenchymal stem-like cells from human endometrium. Hum Reprod 2007;22:2903–11.
24. Schwab KE, Hutchinson P, Gargett CE. Identification of surface markers for prospective isolation of human endometrial stromal colony-forming cells. Hum Reprod 2008;23:934–43.
25. Darzi S, Werkmeister JA, Deane JA, Gargett CE. Identification and characterization of human endometrial mesenchymal Stem/Stromal cells and their potential for cellular therapy. Stem Cells Transl Med 2016;5:1127–32.
26. Coffman LG, Choi YJ, McLean K, Allen BL, di Magliano MP, Buckanovich RJ. Human carcinoma-associated mesenchymal stem cells promote ovarian cancer chemotherapy resistance via a BMP4/HH signaling loop. Oncotarget 2016;7:6916–32.
27. Yang Y, Lin J, Guo S, Xue X, Wang Y, Qiu S, et al. RRM2 protects against ferroptosis and is a tumor biomarker for liver cancer. Cancer Cell Int 2020;20:587.
28. Vulpe CD, Kuo YM, Murphy TL, Cowley L, Askwith C, Libina N, et al. Hephaestin, a ceruloplasmin homologue implicated in intestinal iron transport, is defective in the sla mouse. Nat Genet 1999;21:195–9.
29. Petrak J, Vyoral D. Hephaestin–a ferroxidase of cellular iron export. Int J Biochem Cell Biol 2005;37:1173–8.
30. Manz DH, Blanchette NL, Paul BT, Torti FM, Torti SV. Iron and cancer: recent insights. Ann N Y Acad Sci 2016;1368:149–61.
31. Sun Y, Liu G. Endometriosis-associated ovarian clear cell carcinoma: a special entity? J Cancer 2021;12:6773–86.
32. Torti FM, Torti SV. Regulation of ferritin genes and protein. Blood 2002;99:3505–16.
33. Kawabata H. Transferrin and transferrin receptors update. Free Radic Biol Med 2019;133:46–54.
34. Pantopoulos K. Iron metabolism and the IRE/IRP regulatory system: an update. Ann N Y Acad Sci 2004;1012:1–13.
35. Zhao Y, Li Y, Zhang R, Wang F, Wang T, Jiao Y. The role of erastin in ferroptosis and its prospects in cancer therapy. Onco Targets Ther 2020;13:5429–41.
36. Li S, Xu W, Wang H, Tang T, Ma J, Cui Z, et al. Ferroptosis plays an essential role in the antimalarial mechanism of low-dose dihydroartemisinin. Biomed Pharmacother 2022;148:112742.
37. Yan HF, Zou T, Tuo QZ, Xu S, Li H, Belaidi AA, et al. Ferroptosis: mechanisms and links with diseases. Signal Transduct Target Ther 2021;6:49.
38. Domcke S, Sinha R, Levine DA, Sander C, Schultz N. Evaluating cell lines as tumour models by comparison of genomic profiles. Nat Commun 2013;4:2126.
39. Anglesio MS, Wiegand KC, Melnyk N, Chow C, Salamanca C, Prentice LM, et al. Type-specific cell line models for type-specific ovarian cancer research. PLoS One 2013;8:e72162.
40. Fang X, Cai Z, Wang H, Han D, Cheng Q, Zhang P, et al. Loss of cardiac ferritin H facilitates cardiomyopathy via Slc7a11-mediated ferroptosis. Circ Res 2020;127:486–501.
41. Sun Y, Deng R, Zhang C. Erastin induces apoptotic and ferroptotic cell death by inducing ROS accumulation by causing mitochondrial dysfunction in gastric cancer cell HGC27. Mol Med Rep 2020;22:2826–32.
42. Wang Z, Li M, Liu Y, Qiao Z, Bai T, Yang L, et al. Dihydroartemisinin triggers ferroptosis in primary liver cancer cells by promoting and unfolded protein response-induced upregulation of CHAC1 expression. Oncol Rep 2021;46:240.